LETTER Communicated by Klaus Stiefel

A Simulation Study Investigating the Impact of Dendritic Morphology and Synaptic Topology on Neuronal Firing Patterns

Jen-Yung Chen
jenyungc@ucr.edu
Department of Psychology, Binghamton University, Binghamton, NY 13902-6000, U.S.A.

In the brain, complex information interactions among neurons span several spatial and temporal scales, making it extremely difficult to identify the principles governing neural information processing. In this study, we used computational models to investigate the impact of dendritic morphology and synaptic topology on patterns of neuronal firing. We first constructed Hodgkin-Huxley-type neuron models that possessed dendrites with different morphological features. We then simulated the responses of these neurons to a number of spatiotemporal input patterns. The similarity between neuronal responses to different patterned inputs was effectively evaluated by a novel combination of metric space analysis and multidimensional scaling analyses. The results showed that neurons with different morphological or anatomical features exhibit differences in stimulus-specific temporal encoding and firing reliability. These findings support the idea that in addition to biophysical membrane properties, the dendritic morphology and the synaptic topology of a neuron can play a significant role in neuronal information processing and may directly contribute to various brain functions.

1 Introduction

Neurons, the elemental operating units of the brain, communicate with each other via synapses using a series of discrete electrical signals known as action potentials. A single neuron can receive hundreds to thousands of synaptic inputs, both excitatory and inhibitory, distributed over various locations of its dendrites. These inputs are integrated spatiotemporally at dendrites before they converge onto the cell body. On sufficient depolarization, a new spike train can be generated at the cell body (axon hillock) and transmitted to the following neurons. For decades, neuroscientists have been interested in studying the underlying biological mechanisms that functionally manipulate the input-output relationships of individual neurons. It has been thought that there are reliable computational principles that can quantitatively and logically interpret how information is integrated

and encoded in the brain. Early efforts have primarily focused on how membrane properties of neurons mediate unitary excitatory and inhibitory postsynaptic potentials (EPSP/IPSP) at dendrites (see Gulledge, Kampa, & Stuart, 2005; and Reyes, 2001, for recent reviews).

In addition to biophysical membrane properties, recent evidence has shown that dendritic morphology and synaptic topology can also play a significant role in neuronal information processing. For instance, in the auditory brain stem, neurons with stereotyped bipolar dendrites have been found such that each dendrite receives input from only one ear (Smith & Rubel, 1979). The dendritic morphology of these binaural neurons facilitates the performance of a significant function: that of detecting interaural time differences between auditory stimuli incident on each ear to help localize the source of the sound (Agmon-Snir, Carr, & Rinzel, 1998; Joris, Smith, & Yin, 1998). Another well-characterized example of dendritic computation is the directional selectivity of starbust amacrine cells in the retina. Extracellular recording and calcium imaging have revealed that the local synaptic inputs at a dendrite sum with global signals only when visual stimuli move in the preferred direction across the dendritic tree and not otherwise (Euler, Detwiler, & Denk, 2002; Tukker, Taylor, & Smith, 2004; Vanay & Taylor, 2002). These reports highlighted the potential contribution of dendritic morphology and synaptic topology to neuronal information processing. The goal of the study reported here is to address this issue systematically by computational modeling.

First, we constructed Hodgkin-Huxley-type model neurons with different morphological attributes that mimic the morphological features of individual neurons in the brain. During simulations, the input signals with specific spatial and temporal patterns were sent to these model neurons, and the resulting firing patterns were faithfully recorded. These neuronal firing patterns were further evaluated by a novel combination of quantitative methods, including metric space analysis and multidimensional scaling analyses. The results show that the length of dendrites, the dendritic branching pattern, and the spatial distribution of synaptic inputs can be significantly involved in information integration and further determine the patterns of firing outputs. These results support the idea that in addition to biophysical membrane properties, the morphological and anatomical features of individual neurons may directly contribute to neural coding and various brain functions.

2 Methods

2.1 Model. In this study, three Hodgkin-Huxley types of model neurons from the nucleus of the solitary tract (NTS) were constructed in NEURON (Hines & Carnevale, 1997). In order to systematically assess the impact of dendritic morphology on neuronal firing activities, the morphological variables were set the same across these three model neurons with the

exception of the length of their primary dendrite (750 μm for a large neuron and a branching neuron and 350 μm for a small neuron) and the number of branching points at their primary dendrite (0 for a large neuron and a small neuron and 2 for a branching neuron). Details of the morphological settings are listed in Table 1. The goal was to vary one feature systematically and study its effects while keeping all other features constant.

The membrane properties of these model neurons were obtained from the results of in vitro experiments (Schild et al., 1993). Each compartment in the model neuron contained a fast Na^+ current (I_{Na}), a delayed rectifier current (I_K), a long-lasting Ca^{2+} current (I_{CaL}), a transient outward potassium current (I_A), a Ca^{2+} activated potassium current (I_{KCa}), a delay current (I_D), an inward rectifier current (I_R), a linear leakage current (I_B), an Na^+-Ca^{2+} exchange current (I_{NaCa}), an Na^+-K^+ pump current (I_{NaK}), and a Ca^{2+} pump current (I_{CaP}). Details of the channel kinetics are listed in appendixes A and B. The extracellular concentration of ions ($[Ca^{2+}]_o$, $[Na^+]_o$, $[K^+]_o$) was assumed to be constant. In all model neurons, calcium buffering was also included (see appendix A).

Since the distribution of ion channels can undergo significant change during nervous system development (Maletic-Savatic, Lenn, & Trimmer, 1995; Miyashita & Kubo, 1997), precise channel distributions for most neurons in the brain are still unknown. In this study, the membrane properties, which were distributed evenly across the dendrites and the soma, were tested here. At the axon, only a fast Na^+ current (I_{Na}) and a delayed rectifier current (I_K) were included.

Next, a computational model of an excitatory synapse characterized by several variables, the rising time constant, the decaying time constant, and the reversal potential based on several reports (Chen, Horowitz, & Bonham, 1999; Schild et al., 1993; Wang & Bradley, 1995) was constructed. Their values are listed in appendix B. In addition, two types of connection paradigms, each distinguished by its distribution of synapses across the dendritic tree (dispersive or concentrated), were also examined. The placement of synaptic inputs for these two different paradigms is illustrated in Table 2.

2.2 Metric Space Analysis. In order to examine the similarity of temporal patterns among spike trains, metric space analysis (Victor, 2005; Victor & Purpura, 1996, 1997) was applied here. Using this analysis, a family of metrics could be derived to quantitatively measure the distance (degree of dissimilarity between temporal patterns) between spike trains. The distance between two spike trains was simply represented by the minimum total cost of transforming one spike train into the other through several sequences of elementary steps: moving, inserting, or deleting specific spikes. First, the cost of moving a spike by an amount of time t was counted as qt, where q (sec^{-1}) was the cost of moving a spike per unit time (1 second). Further, each spike that was deleted or added incurred a cost of 1. Based on this algorithm, the costs of all possible sequences to transform one spike

Table 1: Morphological Settings of Three Model Neurons: A Large Neuron, Small Neuron, and Branching Neuron.

Large Neuron	*Small Neuron*	*Branching Neuron*
Primary dendrite *length* = 750 μm; *diam* = 4 μm; Peripheral dendrite *length* = 40 μm; *diam* = 3 μm; Soma *length* = 40 μm; *diam* = 8 μm; Axon *length* = 500 μm; *diam* = 4 μm;	Primary dendrite *length* = 350 μm; *diam* = 4 μm; Peripheral dendrite *length* = 40 μm; *diam* = 3 μm; Soma *length* = 40 μm; *diam* = 8 μm; Axon *length* = 500 μm; *diam* = 4 μm;	First-order primary dendrite *length* = 250 μm; *diam* = 4 μm; Second-order primary dendrite *length* = 250 μm; *diam* = 4 μm; Third-order primary dendrite *length* = 250 μm; *diam* = 4 μm; Peripheral dendrite *length* = 40 μm; *diam* = 3 μm; Soma *length* = 40 μm; *diam* = 8 μm; Axon *length* = 500 μm; *diam* = 4 μm;
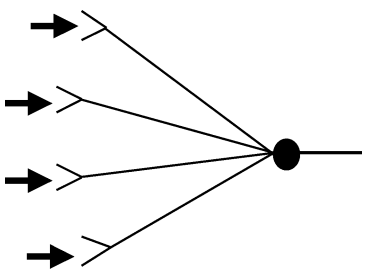	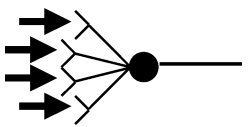	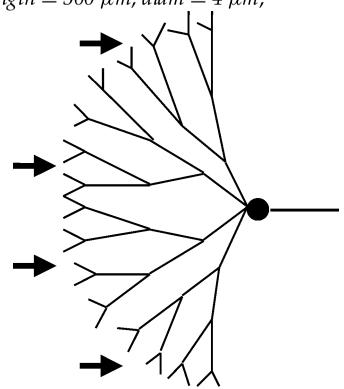

Note: The accuracy of the spatial grid followed the d lambda rule embedded in NEURON with d lambda = 0.1 and f = 100 Hz.

Table 2: Two Types of Synaptic Topology in the Model Neurons.

Dispersive Inputs	Concentrated Inputs
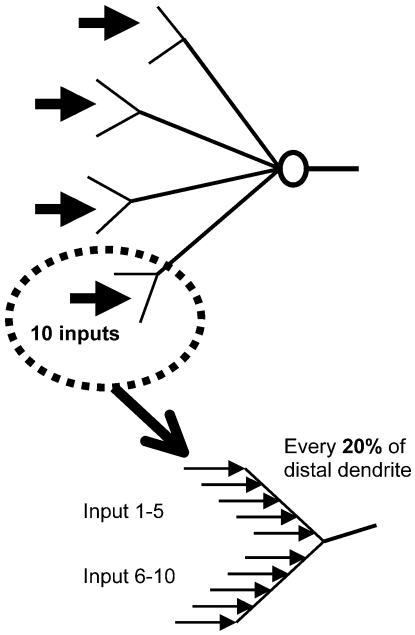	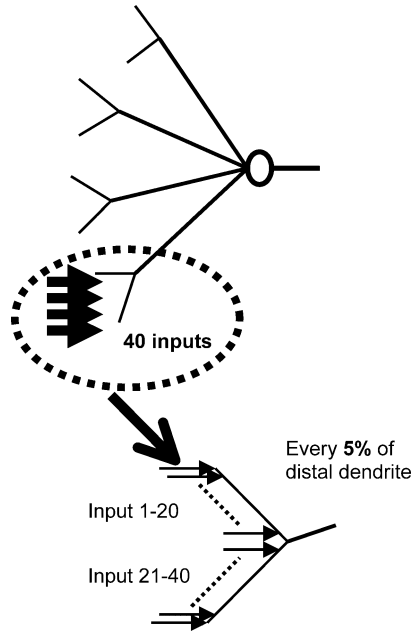

train into the other were calculated, and the sequence that yielded a minimum cost was chosen. In this study, the parameter q was set to 20 (at a temporal precision of 50 ms). Based on this measure, if spiking patterns were to depend on the dendritic morphology, we expect that the distance between patterns generated by different neuron types would be greater than patterns generated by similar neurons. (See Di Lorenzo & Victor, 2003; Di Lorenzo, Chen, & Victor, 2009; and Roussin, Victor, Chen, & Di Lorenzo, 2008, for other examples where metric space analysis was used.)

2.3 Multidimensional Scaling Analyses (MDS). A matrix of pairwise distances between spike patterns was generated using the metric space analysis introduced above. The values of this matrix were then chosen as inputs to multidimensional scaling analyses (MDS) to visualize the underlying relationships among the spike trains in terms of the similarity of their temporal patterns.

MDS provides a geometrical representation of data similarity or dissimilarity and has often been used to visualize the underlying structure of relationships among individual entities or groups of entities under

Table 3: Six Categories of Inputs with Different Frequency (5/40 Hz) or Level of Correlation (Random/Medium Correlated/Highly Correlated).

Categories of inputs (various degree of correlation)	Number of Sets	Length of Each Time Window	First Fixed Time Point at the First Time Window	Mean of Added Poisson Interval
5 Hz random inputs—low correlation	20 sets			
5 Hz medium-correlated inputs	20 sets	200 ms	2050	50 ms
5 Hz highly correlated inputs	20 sets	200 ms	2090	10 ms
40 Hz random inputs—low correlation	20 sets			
40 Hz medium-correlated inputs	20 sets	25 ms	2006.25	6.25 ms
40 Hz highly correlated inputs	20 sets	25 ms	2009.5	3 ms

investigation (Kruskal & Wish, 1978). In the beginning, the objects (entities) were moved around in a space of required dimensions. Then the best fit-configuration of objects in this multidimensional space could be decided after a series of evaluations of how well a particular configuration reproduced the observed distance matrix by simply summing the squared deviations of observed distances (obtained from metric space analysis) from the reproduced distances (obtained from a particular configuration of MDS). In this study, objects, the input or output spike trains, were embedded in a hypothetical space such that the distances from one to another corresponded to the relative similarity of their temporal patterns measured by the metric space analysis. When there were morphology- or anatomy-dependent firing patterns, the spike trains (objects) from the same model neuron or the same anatomical setting would tend to get together and form individual clouds in the MDS space. According to the geometrical configuration of these clouds, new relationships among received inputs and firing outputs can be revealed. The actual orientation of axes in the MDS space is arbitrary. The meaning of an axe can be abstract (interpreted by user). In this study, they are kept as dimension I, dimension II, and dimension III.

2.4 Simulations. Six categories (120 sets) of artificial spike trains were constructed and served as inputs to the model neurons. They are 5/40 Hz Poisson random inputs, 5/40 Hz medium-correlated inputs, and 5/40 Hz highly correlated inputs (see Table 3). Those random inputs were generated using a Poisson process. The correlated inputs were constructed by adding a random interval to a fixed time point in each time window (see Figure 1). Since the level of correlation among input spike trains can be recognized as the level of jitter (synchronization) among them, higher-correlated inputs are made by adding smaller random intervals (lower mean value) to a fixed time point. Detailed information of correlated inputs is listed in Table 3.

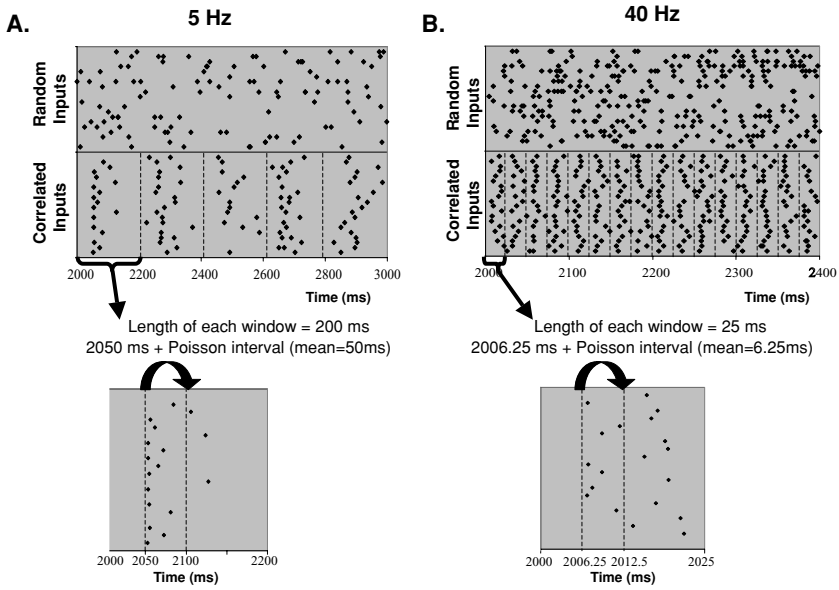

Figure 1: Inputs sent to model neurons could be 5 or 40 Hz random or correlated spike trains. Random spike trains were generated by a Poisson process. Correlated spike trains were generated by adding a Poisson interval at the initial time point to each time window. (A) In a 5 Hz correlated spike train, a series of time windows with length equal to 200 ms (1/5 sec) was first decided. An event (spike) was inserted in each time window by adding a Poisson interval to the initial time point. The initial time point is set at the end of the first quarter of each time window, and the mean of the Poisson interval is set to be equal to a quarter of a time window (50 ms in this case). The raster plots of 5 Hz Poisson random spike trains and 5 Hz medium-correlated spike trains are shown here. (B) A similar idea is applied to generate 40 Hz correlated inputs. Instead of 200 ms, a time window of 40 Hz correlated inputs is set to be 25 ms (1/40 sec). After the initial time points of each time window are decided (at the end of the first quarter of each window), a Poisson interval with mean equal to 6.25 ms (a quarter of 25 ms) is added. The raster plots of 40 Hz random spike trains and 40 Hz medium-correlated spike trains are shown here.

During each run of the simulation, one set of the inputs (that included 40 different spike trains) was assigned to 40 different synapses distributed on the neuron. Each run consisted of an initial 2 seconds of silence followed by a spike train that lasted 5 seconds and another 1 second where no input was presented to the neuron. The timing of individual spikes was recorded from the middle of an axon when the action potential reached a threshold of 10 mV. A total of 800 trials of simulation were conducted. Those

Table 4: Complete List of Simulations Executed in This Study.

Individual Sets of Inputs	Synaptic Topology	Large Cell	Small Cell	Branching Cell
40 Poisson random inputs (5 Hz)	Dispersive	Ran 20 trials (sets)	Ran 20 trials (sets)	Ran 20 trials (sets)
(synaptic weights = 0.01)	Concentrated	Ran 20 trials (sets)	Ran 20 trials (sets)	Ran 20 trials (sets)
40 Poisson random inputs (40 Hz)	Dispersive	Ran 20 trials (sets)	Ran 20 trials (sets)	Ran 20 trials (sets)
(synaptic weights = 0.01)	Concentrated	Ran 20 trials (sets)	Ran 20 trials (sets)	Ran 20 trials (sets)
40 medium correlated inputs (5 Hz)	Dispersive	Ran 20 trials (sets)	Ran 20 trials (sets)	Ran 20 trials (sets)
(synaptic weights = 0.01)	Concentrated	Ran 20 trials (sets)	Ran 20 trials (sets)	Ran 20 trials (sets)
40 medium correlated inputs (40 Hz)	Dispersive	Ran 20 trials (sets)	Ran 20 trials (sets)	Ran 20 trials (sets)
(synaptic weights = 0.01)	Concentrated	Ran 20 trials (sets)	Ran 20 trials (sets)	Ran 20 trials (sets)
40 highly correlated inputs (5 Hz)	Dispersive	Ran 20 trials (sets)		
(synaptic weights = 0.01)	Concentrated	Ran 20 trials (sets)		
40 highly correlated inputs (40 Hz)	Dispersive	Ran 20 trials (sets)		
(synaptic weights = 0.01)	Concentrated	Ran 20 trials (sets)		
4 Poisson random inputs (5 Hz)	Dispersive	Ran 20 trials (sets)	Ran 20 trials (sets)	Ran 20 trials (sets)
(synaptic weights = 1)	Concentrated	Ran 20 trials (sets)	Ran 20 trials (sets)	Ran 20 trials (sets)
4 Poisson random inputs (40 Hz)	Dispersive	Ran 20 trials (sets)	Ran 20 trials (sets)	Ran 20 trials (sets)
(synaptic weights = 1)	Concentrated	Ran 20 trials (sets)	Ran 20 trials (sets)	Ran 20 trials (sets)

trials are summarized in Table 4. In addition, to give a clearer picture of the analysis combining metric space analysis and MDS, a flowchart using 5 Hz random inputs and 5 Hz correlated inputs as an example is presented in Figure 2.

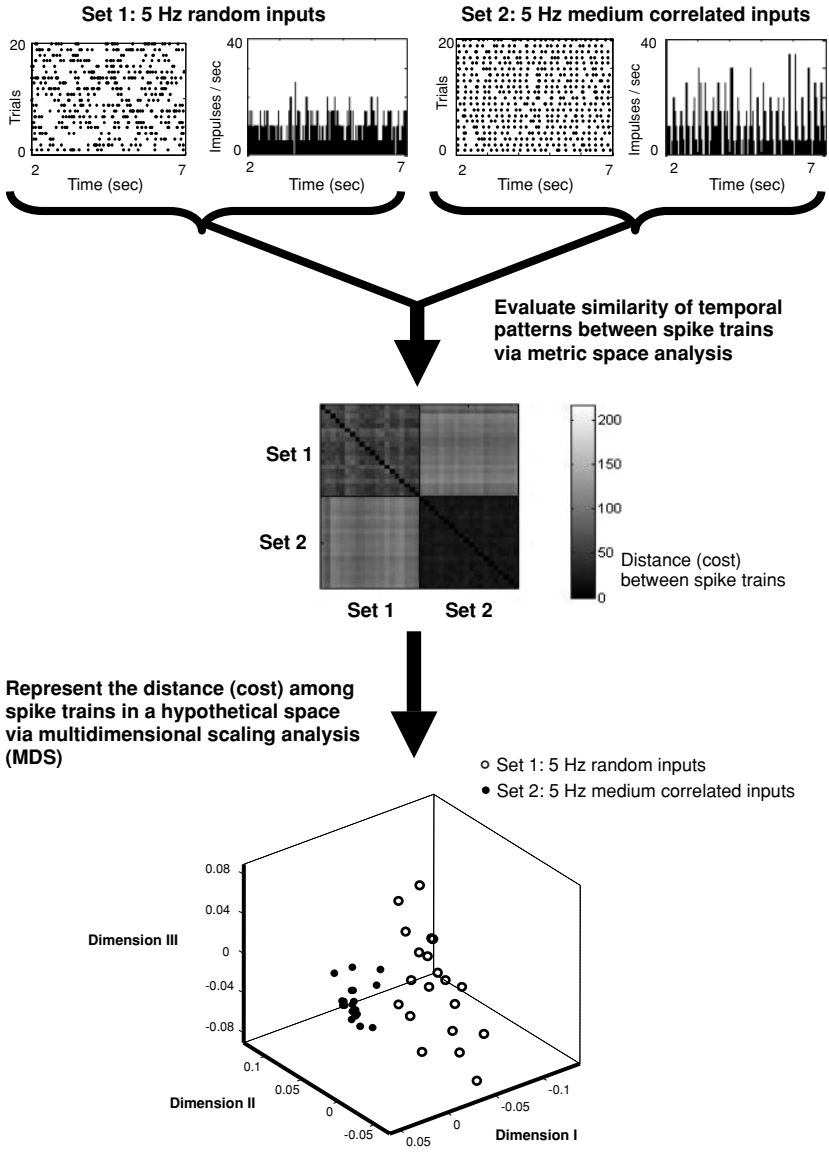

3 Results

3.1 Model Neurons Demonstrate an Ability to Integrate Complex Synaptic Inputs. Figures 3 and 4 show the poststimulus time histograms (PSTH) used to illustrate neuronal responses in relation to the input spike trains they receive. No apparent pattern was found as model neurons received low-frequency (5 Hz) random inputs (see Figure 3A). However, when the neurons received medium-correlated inputs at the same frequency (5 Hz), a clear resonance (see Figure 3B) was observed in all model neurons regardless of differences in their dendritic morphology and synaptic topology. In Figure 4A, a resonance was seen in responses to 40 Hz random inputs only if these inputs were distributed locally. Further, in Figure 4B, 40 Hz medium-correlated inputs resulted in resonance across all neurons. The resonance became stronger as the inputs were distributed more widely.

Next, using metric space analysis and MDS, the neuronal response patterns were compared with the patterns of random inputs they received. In Figure 5, each point in the MDS plot represents a 5 second spike train with random inputs being shown by the open circles and the firing outputs by the filled circles. In Figure 5A, for instance, 20 open circles represent the 5 Hz random inputs received by a large model neuron, and 20 filled circles indicate its firing outputs. Here, the firing outputs form a cluster (cloud) that can be separated from the cloud consisting of the random inputs it received. Such clustering was evidenced in all model neurons that received dispersive low- (5 Hz) or high- (40 Hz) frequency random inputs (see Figures 5A through 5F). This geometrical structure suggests that neurons can reliably regulate their firing patterns even when inputs arrive randomly and are distributed widely across the dendritic tree. Furthermore, the outputs in Figures 5B, 5D, and 5F clustered closely compared to those in Figures 5A,

Figure 2: Flowchart introducing the procedure combining metric space analysis and multidimensional scaling analyses (MDS). First, the similarity of temporal patterns among spike trains is evaluated by metric space analysis. Then the outcomes of metric space analysis are used as inputs to MDS. After MDS, a multidimensional MDS plot can be acquired with each object in this space representing an individual spike train. The relative distance among them simply represents the degree of similarity of their temporal patterns. Spike trains displaying more similar temporal patterns are closer to each other in this MDS plot. When 5 Hz medium-correlated spike trains and 5 Hz random spike trains are used as an example, the temporal patterns of 5 Hz correlated spike trains are proved to be more similar to each other than 5 Hz random spike trains in this figure. This is evidenced by a more condensed cloud (filled circles) consisting of 5 Hz correlated spike trains in this MDS plot.

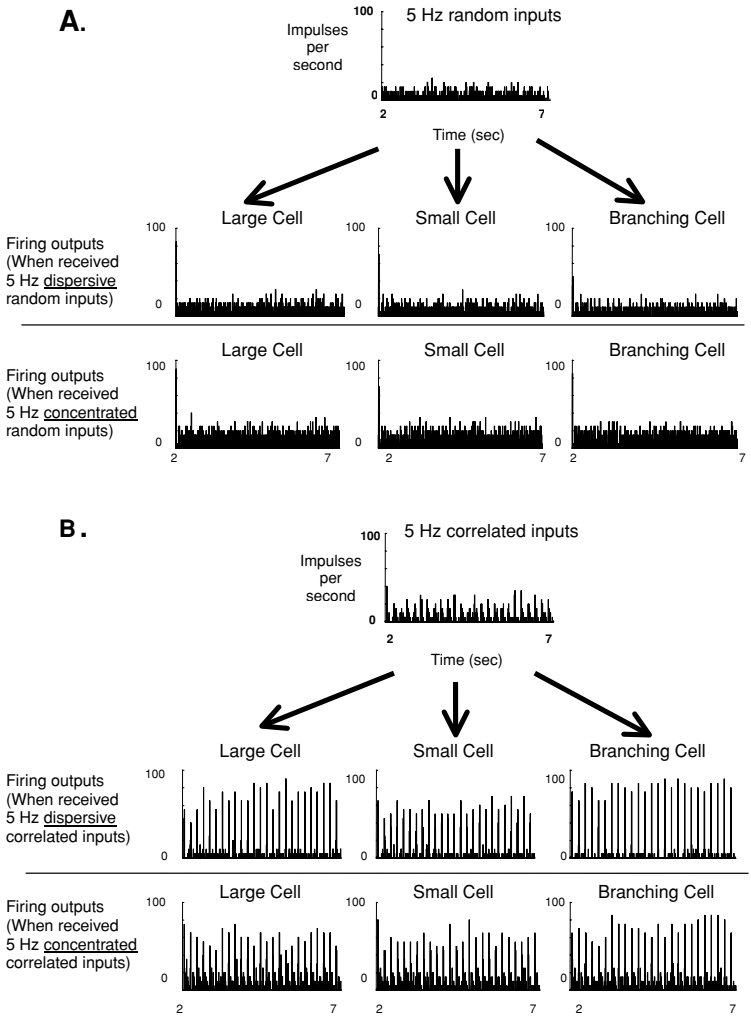

Figure 3: (A) PSTHs of 5 Hz random inputs and the neuronal responses they evoked. No special response pattern is found in these cases. (B) PSTHs of 5 Hz medium-correlated inputs and the neuronal responses they evoked. Clear resonance can be seen in all neurons.

5C, and 5E, indicating that output patterns tend to be more reliable (reproducible) as the input frequency gets higher.

3.2 Effects of Dendritic Morphology on Temporal Firing Patterns. In order to explore if morphological features of dendrites can affect neuronal firing activity, the firing patterns from three model neurons were compared to each other as they received the same sets of inputs. In Figures 6A

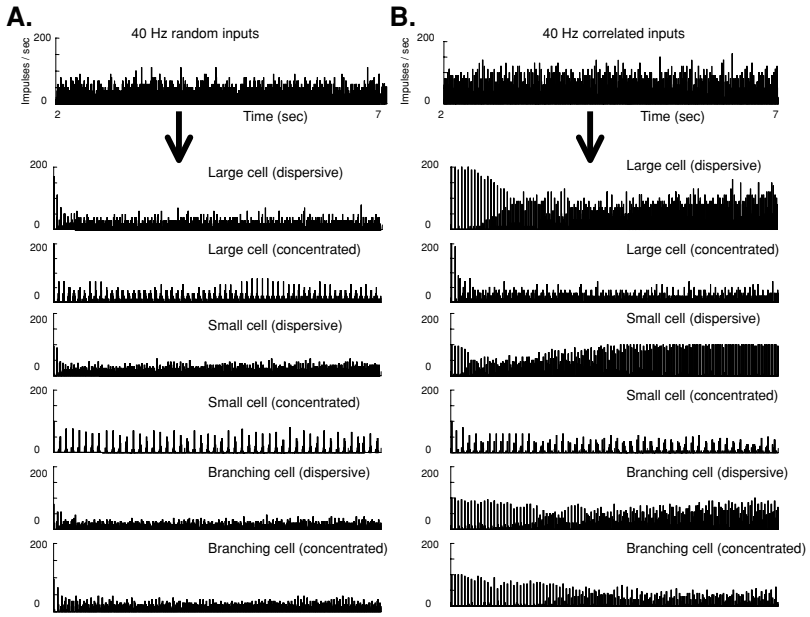

Figure 4: (A) PSTHs of 40 Hz random inputs and neuronal responses they evoked. Neurons are found to be able to regulate a high frequency of random inputs and generate resonant outputs, especially when the synaptic inputs distribute closer to each other. (B) PSTHs of 40 Hz medium-correlated inputs and the neuronal responses they evoked. Resonant firing outputs can be seen in all cases. Moreover, it is found that the degree of resonance can change dramatically in large neurons and small neurons as the synaptic topology changes from a dispersive to a concentrated distribution.

and 6B, the similarity of neuronal firing patterns was investigated as three model neurons received the same sets of 5 Hz or 40 Hz random inputs. First, all three neurons generated very similar firing patterns in response to the low frequency (5 Hz) of random inputs as evidenced by the extensive overlap among the corresponding clusters (circle, dot, and cross) in Figure 6A. In Figure 6B, an increase in frequency of inputs (40 Hz) led to dramatically different outcomes. The firing patterns generated by the three model neurons clearly separated from each other. This striking change suggests a morphology-dependent impact on neuronal firing patterns. That is, different dendritic morphology can perform as different arithmetic, which decides the way of neuronal information integration at dendrites and further determines the temporal patterns of firing outputs. This morphology-dependent consequence is more apparent as the neurons receive higher frequency of inputs. Similar results were observed as neurons received 5 Hz or 40 Hz medium-correlated inputs (see Figures 6C and 6D).

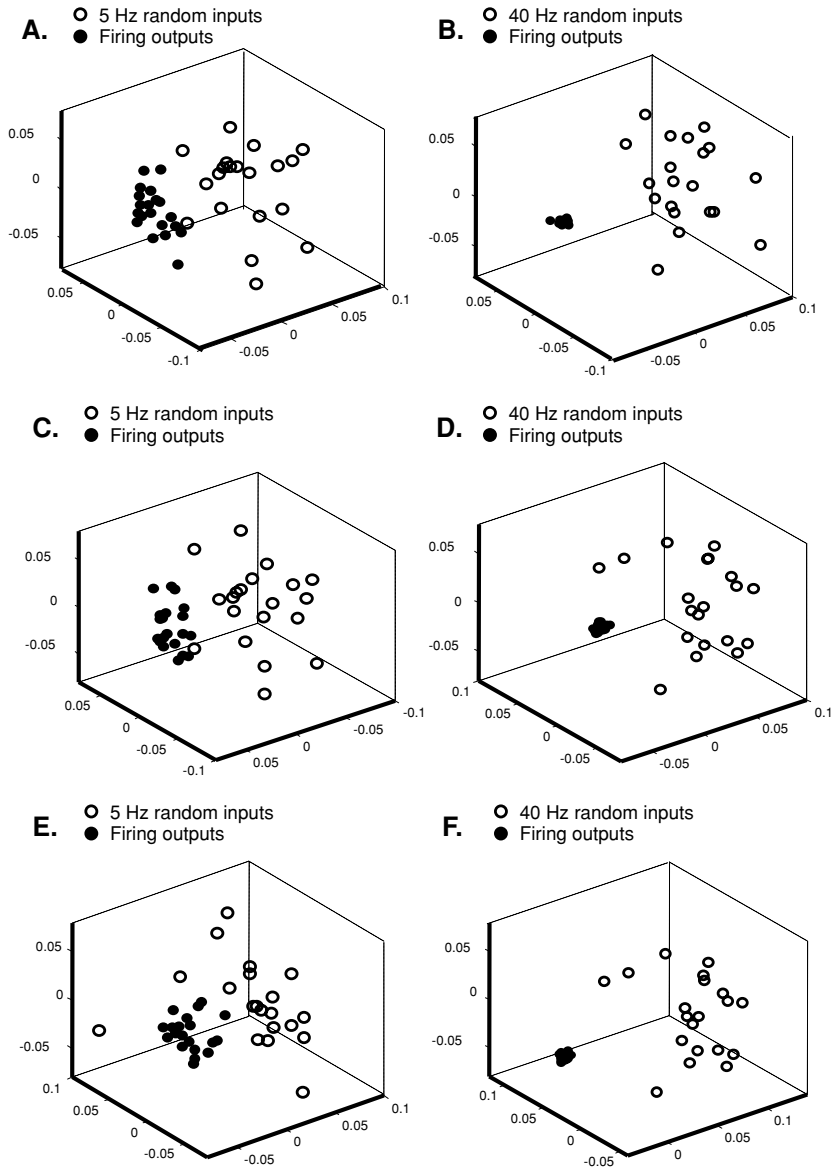

3.3 Effects of Synaptic Topology on Temporal Firing Patterns. Next, the impact of anatomical features on neuronal firing patterns was assessed. As shown in Table 2, two types of connections were tested here. During the simulations, each model neuron received the same set of inputs through a dispersive or a concentrated distribution of synapses. The response firing patterns were then systematically evaluated by metric space analysis and

MDS. The results are shown in Figure 7. In general, when the distribution of synaptic inputs changed, a new cluster of firing outputs in the MDS plot was formed. One exceptional case is observed in Figure 7F. In this figure, when a high frequency of random inputs was sent to a branching neuron, all firing patterns were very similar regardless of the distribution of synapses. In addition, a highly reliable firing pattern (indicated by an extremely dense cloud in a MDS plot) was commonly observed as neurons received concentrated high-frequency inputs (see Figures 7B, 7D, and 7F). According to these results, the synaptic topology can also involve neuronal information processing, and this processing is frequency dependent.

3.4 Impact of Level of Correlation of Inputs. Next, we explored the dependence of output patterns on the correlation of input patterns. Six categories of input patterns with different frequency and different level of correlation were sent to large model neurons via dispersive or concentrated distribution of synapses. These six categories of inputs are listed in Table 3. Their raster plots are shown in Figures 8A and 9A.

The impacts of correlation of input patterns on neuronal firing patterns are shown in Figures 8B and 9B. In Figure 8B, when inputs were at low frequency (5 Hz in this case), inputs with different levels of correlation generally evoked distinguishable patterns of outputs (separable clouds in the MDS plot). The output patterns evoked by higher-correlated inputs are usually more reliable (indicated by an extremely condense cloud in the MDS plot). Furthermore, it was noticed that as a neuron received low-frequency inputs, variation of the synaptic topology (dispersive or concentrated) did not change the configuration of firing outputs in the MDS plots. Interestingly, when the input frequency was increased to 40 Hz, the configurations

---

Figure 5: Six MDS plots that introduce the similarity of temporal patterns of particular inputs (5 Hz or 40 Hz random inputs) and the firing outputs they evoked in each model neuron. The input spike trains were delivered to each neuron via dispersive distribution of synapses. (A) An MDS plot containing 5 Hz random inputs (○) and the firing outputs they evoked (●) in a large neuron. (B) An MDS plot showing 40 Hz random inputs (○) and the firing outputs they evoked (●) in a large neuron. (C) An MDS plot exhibiting 5 Hz random inputs (○) and the firing outputs they evoked (●) in a small neuron. (D) An MDS plot containing 40 Hz random inputs (○) and the firing outputs they evoked (●) in a small neuron. (E) An MDS plot containing 5 Hz random inputs (○) and the firing outputs they evoked (●) in a branching neuron. (F) An MDS plot showing 40 Hz random inputs (○) and the firing outputs they evoked (●) in a branching neuron. In these MDS plots, the clusters consisting of input and output spike trains are clearly separable. This particular arrangement of spike trains in these MDS plots indicates that neurons are able to systematically regulate the input signals they receive and generate reliable firing patterns. This performance is apparent as a neuron receives a higher frequency of inputs.

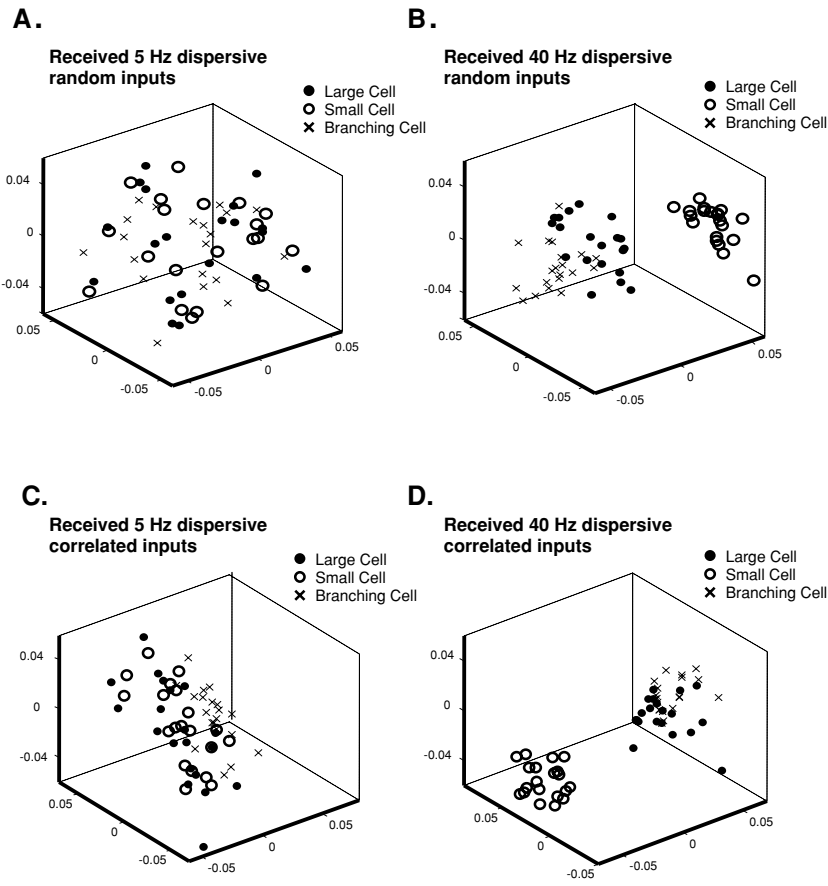

Figure 6: Two sets of MDS plots shown to elucidate the impact of dendritic morphology on neuronal firing patterns. Comparison of the temporal patterns across three different model neurons as they received exactly the same sets of dispersive inputs shows a change of configuration in these MDS plots. Four sets of inputs were sent to model neurons: (A) 5 Hz random inputs, (B) 40 Hz random inputs, (C) 5 Hz medium-correlated inputs, and (D) 40 Hz medium-correlated inputs. In these MDS plots, three symbols are used to represent firing outputs of three different model neurons respectively: • for a large neuron, ○ for a small neuron, and × for a branching neuron. It is found that when neurons received a lower frequency of inputs (5 Hz in *A* and *C*), they generated quite similar firing patterns regardless of the differences in their dendritic morphology. However, as the frequency of inputs increases to 40 Hz (in *B* and *D*), the clusters (clouds) of output spike trains acquired from different model neurons become more distinguishable. Thus, the morphology-dependent information processing at dendrites is shown to be frequency dependent.

of firing outputs in the MDS plots dramatically changed as the synaptic topology changed. In Figure 9B (right), firing patterns became quite similar (overlap among clouds) as the 40 Hz inputs were delivered to the neuron by a concentrated distribution of synapses.

3.5 Impact of Number of Inputs. Membrane potential traces recorded from the soma of a large model neuron when the number of inputs was reduced from 40 to 4 and the strength of synaptic conductance was increased from 0.01 to 1 are shown in Figures 10A and 10B. When the neuron received fewer though stronger inputs, the membrane potential trace was less noisy (see Figure 10A) than the one recorded when a large number of comparatively weak inputs were presented (see Figure 10B). In the former case, the impact of dendritic morphology and synaptic topology on neuronal firing patterns (see Figures 10C and 10D) was found to be similar to our results presented in previous sections (see Figures 6 and 7). Thus, as the number of inputs and the strength of conductance changed, the impacts of dendritic morphology and synaptic topology on neuronal firing patterns are similar (showing similar configurations in MDS plots).

4 Discussion

Identifying the principles of neural computation in the brain is a challenging task due to the number of biological variables that can interact with each other dynamically at various spatial and temporal scales. Fortunately, the development of a computational modeling technique offers an effective way to resolve this difficulty. When current is injected into the soma, various firing patterns can be reproduced from the reconstructed neocortical model neurons (Mainen & Sejnowski, 1996). In the current study, which used a different simulation strategy, multiple model neurons with simplified morphological structures were constructed first. Then the changes in neuronal responses caused by specific morphological or anatomical features were systematically evaluated using a novel combination of metric space analysis and MDS. These quantitative methods together provide a more rigorous way to investigate neuronal firing activities than conventional representations (e.g., raster plot or PSTH) and measures (e.g., discharging rate or distribution of interspike interval). Our results reveal the contribution of dendritic morphology and synaptic topology on neuronal information processing (neural coding). These ideas are consistent with several recent experiments discussed below:

• *Dendritic morphology and synaptic topology can be very specific.* Recent progress in our understanding of dendrite growth and axon guidance shows that both intracellular and extracellular molecular mechanisms, in conjunction with ongoing synaptic activity, are involved in the process of dendritic branching and targeting during nervous system development (Cline, 2001;

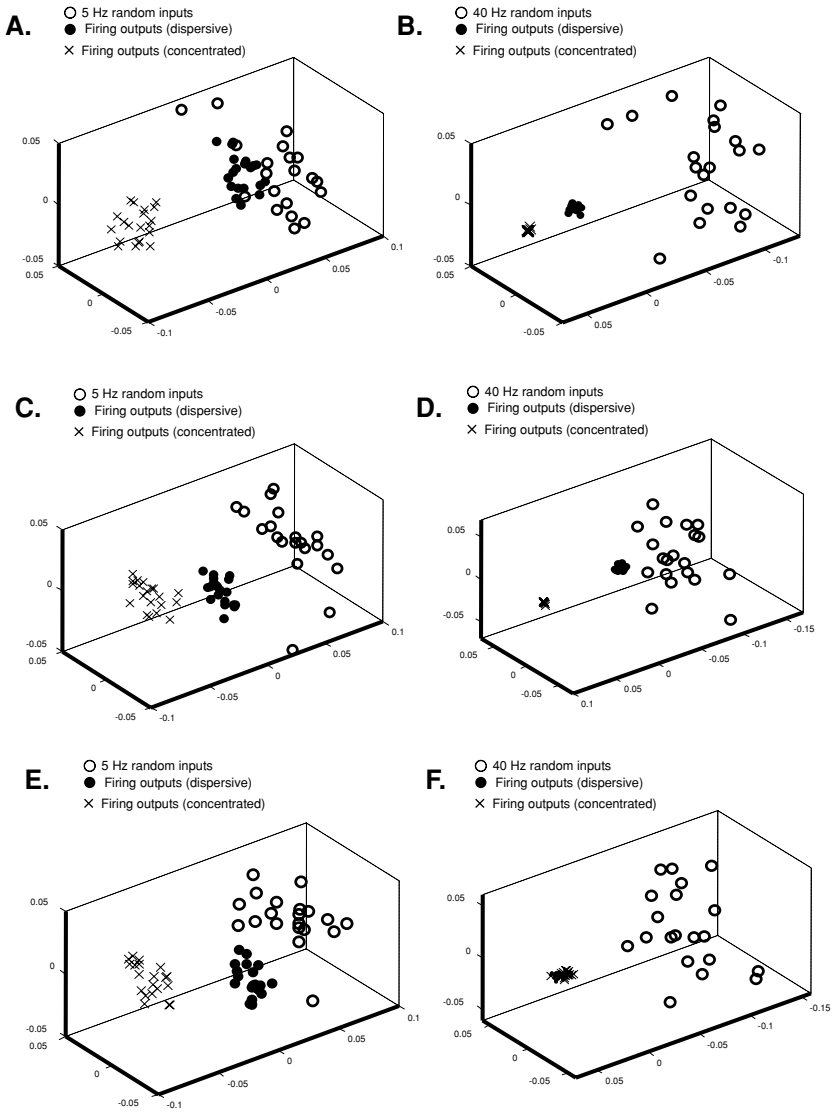

Gao, Brenman, Jan, & Jan, 1999; Gao, 2007; Jan & Jan, 2003; McAllister, 2000; Scott & Luo, 2001; Wong & Ghosh, 2002). Furthermore, the formation of synapses on these emerging neurons is precisely located and predetermined by genetic instruction (Benson, Colman, & Huntley, 2001; Shen & Bargmann, 2003; Shen, 2004; Somogyi, Tamas, Lujan, & Buhl, 1998). Taken together, these findings lend credence to the position that dendritic morphology and synaptic topology in the brain may be more intricately planned than previously thought. Such specific organization highlights the potential

contribution of dendritic morphology and synaptic topology as key features in neuronal information processing.

• *Dendritic arithmetic.* For decades, neuroscientists have devoted considerable effort to deriving principles of dendritic computation. Two modes of integrating information, each related to the dendritic morphology and synaptic topology, have been observed (Carter, Soler-Llavina, & Sabatini, 2007; Poirazi, Brannon, & Mel, 2003; Polsky, Mel, & Schiller, 2004). First, when high-frequency synchronous inputs activate a restricted portion of the local dendrite, a nonlinear summation of inputs was observed. The threshold of local dendritic spikes increase in a manner that prevents subsequent spikes (Ariav, Polsky, & Schiller, 2003; Gasparini, Migliore, & Magee, 2004; Gasparini & Magee, 2006; Poirazi et al., 2003; Polsky et al., 2004). In contrast, spatially distributed inputs were found to sum linearly, making the neuron more sensitive to the changes of input frequency and timing (Ariav et al., 2003; Gasparini & Magee, 2006; Poirazi et al., 2003; Polsky et al., 2004). These results illustrate several fundamental computational principles regarding the integration of information at dendrites. In order to connect these computational principles to higher-level brain functions, the performance of neuronal computation in a longer time period was investigated in this study (temporal patterns of 5 seconds spike trains). Our simulation results highlight the potential contribution of dendritic morphology and synaptic topology on neuronal computations. Structural characteristics may directly or indirectly contribute to various brain functions.

• *From "form" to "function."* CA1 pyramidal neurons can produce different firing patterns associated with different information integration modes at their dendrites (Gasparini & Magee, 2006). Different modes of information integration at the dendrites can be independently engaged by different behavioral states in animals. For instance, a linear integration mode at dendrites can be associated with theta states, during which a neuron increases its firing rate and shifts its spike timing forward. In addition, a nonlinear

---

Figure 7: In order to realize the impact of synaptic topology on neuronal firing patterns, firing outputs from individual neurons as they receive the same sets of inputs via different synaptic topology (dispersive or concentrated) are investigated. (A) A large neuron receives 5 Hz dispersive or concentrated random inputs. (B) A large neuron receives 40 Hz dispersive or concentrated random inputs. (C) A small neuron receives 5 Hz dispersive or concentrated random inputs. (D) A small neuron receives 40 Hz dispersive or concentrated random inputs. (E) A branching neuron receives 5 Hz dispersive or concentrated random inputs. (F) A branching neuron receives 40 Hz dispersive or concentrated random inputs. In general, different synaptic topology evokes different firing patterns. One exception is observed in F as a branching neuron receives a high frequency of inputs. In addition, it is found that firing patterns are commonly more reliable when neurons receive a higher frequency of concentrated inputs. This is indicated by extremely condense clouds of $\times$ in B, D, and F.

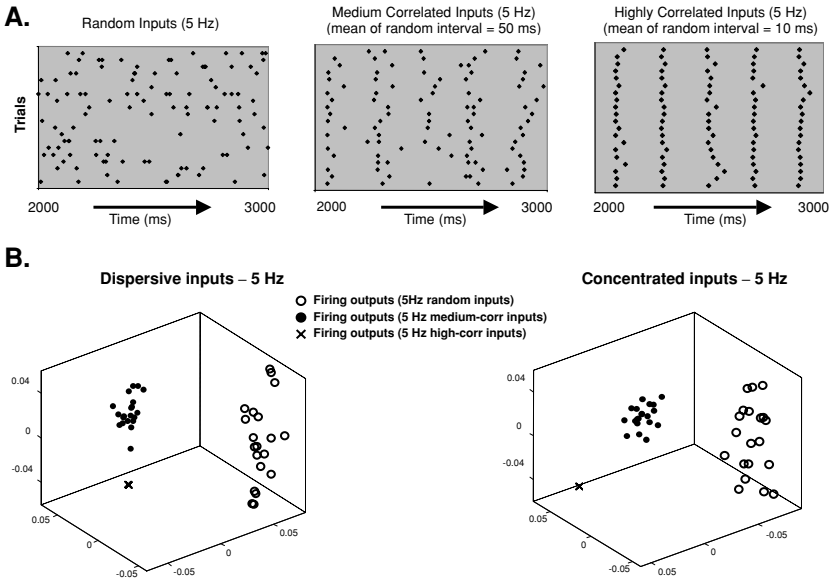

Figure 8: Three categories of 5 Hz inputs with different levels of correlation were constructed and sent to model neurons to explore the dependence of firing outputs on correlation of input. (A) Raster plots of three categories of inputs: 5 Hz random inputs, 5 Hz medium-correlated inputs, and 5 Hz highly correlated inputs. (B) Two MDS plots show the impact of input correlation (5 Hz) on neuronal firing patterns through dispersive (left) or distributed (right) connecting paradigm. Overall, higher correlated inputs evoked more reliable firing patterns. In addition, variation of synaptic topology did not change the configuration of outputs in the MDS plot.

integration mode at the dendrites can be associated with sharp-wave states during which a neuron receives more synchronous and concentrated inputs and produces well-timed outputs. Thus, different modes of information transmission exist in the nervous system, each performing a different computational function and serving a different behavioral state. However, more experiments, relying on advanced in vivo optical recording from individual neurons during different behavioral states of awake animals, may be necessary to prove this idea.

• *Temporal firing characteristics convey more information than discharging frequency during neuronal information processing.* In the awake state, animals often respond to stimuli or make decisions in less than a few hundred milliseconds. The completion of complex cognitive tasks in a short period requires highly precise and reliable patterns of neuronal spiking. In the taste system, for instance, in vivo studies (Di Lorenzo & Victor, 2003; Roussin et al., 2008) have found that different taste stimuli evoke distinguishable temporal responses in the gustatory NTS. These responses are

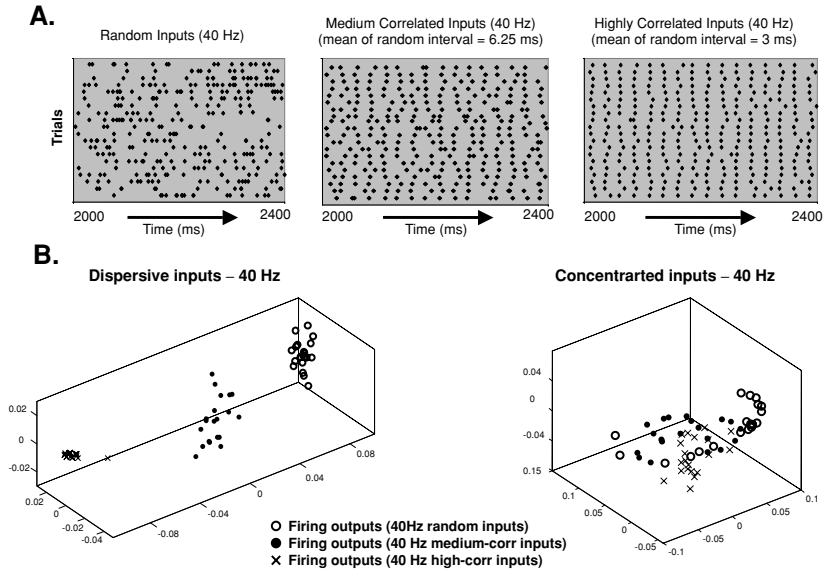

Figure 9: Another three categories of 40 Hz inputs with different levels of correlation were constructed and sent to model neurons to explore the dependence of firing outputs on correlation of input. (A) Raster plots of three categories of inputs: 40 Hz random inputs, 40 Hz medium-correlated inputs, and 40 Hz highly correlated inputs. (B) Two MDS plots show the impact of input correlation (40 Hz) on neuronal firing patterns through a dispersive (left) or distributed (right) connecting paradigm. It was found that the configuration of outputs in these MDS plots dramatically changed as the connecting paradigm changed. When inputs were sent to a model neuron by a concentrated distribution of synapses, the neuron generated quite similar output patterns regardless of the level of correlation of inputs.

highly reproducible in repeated trials. It was established using metric space analysis that information contained in the temporal firing characteristics was significantly higher than information contained in the average discharge rate. Similar experiments emphasizing the significance of temporal firing precision during neuronal information processing have also been reported in other sensory systems (Agmon-Snir et al., 1998; Joris et al., 1998; Lestienne, 2001; Singer, 1999; Stopfer & Laurent, 1999).

In sum, by using computational modeling technique along with novel combination of metric space analysis and MDS, the results of this study show that there are morphology- and anatomy-dependent computational mechanisms that influence the spiking activity of individual neurons. In the near future, it will be critical to see how these morphology- and anatomy-dependent mechanisms contribute to the network level of computations and eventually to various brain functions.

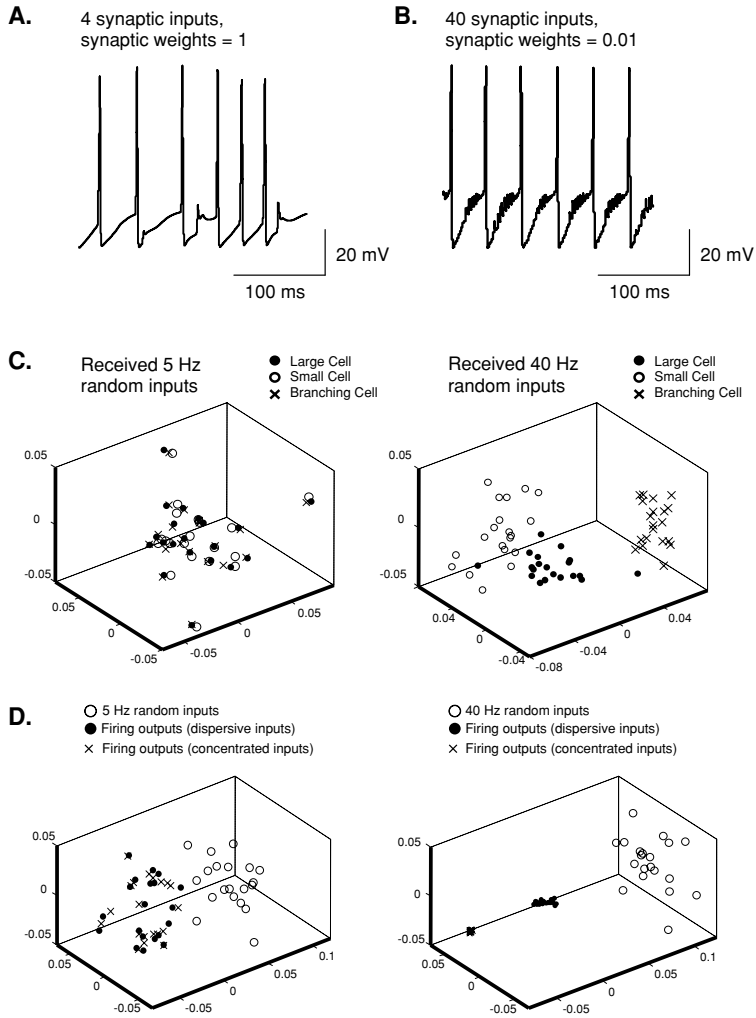

Figure 10: The somatic membrane potential traces of a large model neuron are introduced in *A* and *B*. (A) A large model neuron receives 4 synaptic inputs with synaptic weights equal to 1. (B) A large model neuron receives 40 synaptic inputs with synaptic weights equal to 0.01. (C) The impact of dendritic morphology on neuronal firing patterns was evaluated as all three model neurons received 4 synaptic inputs with synaptic weights equal to 1. The results are consistent with Figure 6, showing morphology- and frequency-dependent firing activities. (D) The impact of synaptic topology on neuronal firing patterns was systematically evaluated. In general, the outcomes are consistent with the results illustrated in Figure 7 except that extensive overlap between two clouds of firing outputs evoked by 5 Hz random inputs is observed here in *D* (left).

Appendix A: List of Channel Kinetics.

Currents	Kinetic Models	State Variables
Fast sodium current ($\mathbf{I}_{\mathrm{Na}}$)	$\mathbf{I}_{Na} = \overline{g}_{\mathrm{Na}}\, m^3\, h\, (V - E_{\mathrm{Na}})$	$\alpha_{\mathrm{m}} = \frac{0.36(V+35)}{1-\exp[-(V+35)/3]}$ $\beta_{\mathrm{m}} = \frac{-0.4(V+53)}{1-\exp[(V+53)/20]}$ $\tau_{\mathrm{m}} = 0.05+(2/(3.488^{*}(\alpha_{\mathrm{m}}+\beta_{\mathrm{m}})))$ $\mathrm{m}\infty = \alpha_{\mathrm{m}}/(\alpha_{\mathrm{m}} + \beta_{\mathrm{m}})$ $\tau_{\mathrm{h}} = 1.15\exp[-(0.055)^2(\mathrm{V} + 29.62)^2] + 0.15$ $\mathrm{h}\infty = \frac{1}{1+\exp[(V+29.62)/5.035]}$
Long-lasting calcium current ($\mathbf{I}_{\mathrm{CaL}}$)	$\mathbf{I}_{CaL} = \overline{g}_{\mathrm{CaL}}\, d^2 f (V - E_{Ca})$	$\tau_{\mathrm{d}} = \frac{1}{0.3426\exp(0.0925V)+1.8818\exp(-0.00732V)} + 0.1$ $\mathrm{d}\infty = \frac{1}{1+\exp[-(V+2.8)/9.85]}$ $\tau_{\mathrm{f}} = \frac{1}{0.2419\exp(0.145V)+0.0434\exp(-0.02013V)}$ $\mathrm{f}\infty = \frac{1}{1+\exp[(V+14.6)/4.5]}$
Delay rectifier current ($\mathbf{I}_{\mathrm{K}}$)	$\mathbf{I}_K = \overline{g}_{\mathrm{K}}\, n^2 (V - E_{\mathrm{K}})$	$\tau_{\mathrm{n}} = 60\exp[-(0.027)^2(V + 32)^2] + 4$ $\mathrm{n}\infty = \frac{1}{1+\exp[(V-7.18701)/(-11.77468)]}$
Early transient outward potassium current ($\mathbf{I}_{\mathrm{A}}$)	$\mathbf{I}_A = \overline{g}_{\mathrm{A}}\, p^3\, (0.5q_1 - 0.5q_2)\, (V - E_{\mathrm{K}})$	$\tau_p = 5.5\exp[-(0.022)^2(V + 65)^2] + 1$ $\mathrm{P}\infty = \frac{1}{1+\exp[(V+51.83144)/(-13.80238)]}$ $\mathrm{q}_1\infty = \frac{1}{1+\exp[(V+73)/4.66667]};\ \tau_{q1} = 70$ $\mathrm{q}_2\infty = \frac{1}{1+\exp[(V+73)/4.66667]};\ \tau_{q2} = 550$
Slowly inactivating delay current ($\mathbf{I}_{\mathrm{D}}$)	$\mathbf{I}_{\mathrm{D}} = \overline{g}_D\, x^3\, y(V - E_K)$	$\tau_{\mathrm{x}} = 5.5\exp[-(0.022)^2(V+ 65)^2] + 1$ $\mathrm{x}\infty = \frac{1}{1+\exp[(V+31.83144)/(-13.13572)]}$ $\tau_{\mathrm{y}} = 6500,$ $\mathrm{y}\infty = \frac{1}{1+\exp[(V+63)/4.66667]}$

Appendix A: (Continued).

Currents	Kinetic Models	State Variables
Calcium-activated potassium current ($\mathbf{I}_{\mathrm{Kca}}$)	$\mathbf{I}_{\mathrm{Kca}} = \overline{g}_{KCa}\, c(V - E_{\mathrm{K}})$	$\alpha_C = 7.5\,[\mathrm{Ca}^{2+}]\,\exp[(V + 20)/24]$ $\beta_C = 0.2\,\exp[(V + 20)/(-24)]$
Inward rectifier current ($\mathbf{I}_{\mathrm{R}}$)	$\mathbf{I}_{\mathrm{R}} = \overline{g}_{\mathrm{R}}\, \frac{(V - Ek - 36)}{1+\exp[(V - Ek + 140)ZF/RT]}$	
Background current ($\mathbf{I}_{\mathrm{NaB}}$, $\mathbf{I}_{\mathrm{KB}}$)	$\mathbf{I}_{\mathrm{NaB}} = \overline{g}_{Na\,B}(V - E_{\mathrm{Na}})$ $\mathbf{I}_{\mathrm{KB}} = \overline{g}_{K\,B}(V - E_{\mathrm{K}})$	
Sodium-calcium exchange current ($\mathbf{I}_{\mathrm{NaCa}}$)	$\mathbf{I}_{\mathrm{NaCa}} = K^{*}_{NaCa}(DF_{in} - DF_{out})/\mathrm{S}$	$\mathrm{S} = 1 + D_{\mathrm{NaCa}}\,([Ca^{2+}]_{\mathrm{i}}\,[Na^{+}]_{\mathrm{o}}{}^{r} + [Ca^{2+}]_{\mathrm{o}}\,[Na^{+}]_{\mathrm{i}}{}^{r})$ $DF_{in} = [\mathrm{Ca}^{2+}]_{\mathrm{o}}\,[Na^{+}]_{\mathrm{i}}{}^{r}\,\exp(\frac{(r-2)\gamma VF}{RT})$ $DF_{out} = [Ca^{2+}]_{\mathrm{i}}\,[Na^{+}]_{\mathrm{o}}{}^{r}\,\exp(\frac{(r-2)(\gamma-1)VF}{RT})$
Calcium pump current ($\mathbf{I}_{\mathrm{CaP}}$)	$\mathbf{I}_{\mathrm{CaP}} = \bar{I}_{\mathrm{CaP}}{}^{*}\,(\frac{[Ca^{2+}]_i}{[Ca^{2+}]_i + K_{M.Ca\,P}})$	
Sodium-potassium pump current ($\mathbf{I}_{\mathrm{NaK}}$)	$\mathbf{I}_{\mathrm{NaK}} = \bar{I}_{\mathrm{NaK}}{}^{*}\,(\frac{[Na^{+}]_i}{[Na^{+}]_i + K_{M.Na}})^{*}$ $(\frac{[K^{+}]_o}{[K^{+}]_o + K_{M.K}})^{*}\,(\frac{V+150}{V+200})$	
Calcium dynamics	$O_{\mathrm{C}} = \mathrm{k_U}\,[\mathbf{Ca}^{2+}]_{\mathrm{i}}{}^{*}\,(1 - O_{\mathrm{C}}) - K_{\mathrm{R}}\,O_{\mathrm{C}}$ $[Ca^{2+}]_{\mathrm{i}} = (I_{Ca}\ /\ 2V_{Ca}\,F) - (n[B]_{\mathrm{i}}\,O_{\mathrm{C}}{}')$	

Source: Schild et al. (1993).

Appendix B: Values of Biophysical Variables.

- Resting membrane potential (– 42.11630 mV)
- $E_{Na} = 75$ mV, $E_K = -80$ mV, $E_{CaL} = 50$ mV
- $\overline{g}_{Na} = 0.5$ uS, $\overline{g}_{CaL} = 0.075$ uS
  $\overline{g}_K = 1.1$ uS, $\overline{g}_A = 0.205$ uS
  $\overline{g}_D = 0.3$ uS, $\overline{g}_R = 0.1$ uS
  $\overline{g}_{Kca} = 0.185$ uS, $\overline{g}_{NaB} = 0.0009315$ uS
  $\overline{g}_{KB} = 0.0009935$ uS
- Membrane capacitance $C_m = 0.052$ nF
- $\overline{I}_{NaK} = 0.15$ nA, $\overline{I}_{CaP} = 0.01$ nA
- [Na]$o = 154$ mM, [Na]i $= 8.71$ mM
  [K]$o = 5.9$ mM, [K]$i = 155$ mM
  [Ca]$o = 2.4$ mM
- $F = 96{,}500$ C mol^{-1}
  $R = 8314$ J kg^{-1} mol^{-1} K^{-1}
  $T = 310$ K, $Z = 1$
- $V_{Ca} = 2003^{*}\ 10^{-12}$ cm^3
- $D_{NaCa} = 0.05$ mM^{-4},
- $K_{NaCa} = 0.00016$ nA mM^{-4}
  $K_{M.CaP} = 0.0005$ mM
  $K_{m.Na} = 5.46$ mM
  $K_{M.K} = 0.621$ mM
- $[B]_i = 0.04$ mM
- $K_U = 100$ mM^{-1} ms^{-1}
- $K_R = 0.238$ ms^{-1}
- $r = 4$, $n = 4$, $\gamma = 0.5$
- Initial value of state variables:
  $m = 0.041904$, $h = 0.923234$
  $n = 0.015467$, $d = 0.018110$
  $f = 0.998023$, $p = 0.666418$
  $x = 0.311018$, $y = 0.056171$
  $q1 = 0.004915$, $C = 0.002932$
  $q2 = 0.008894$, $Oc = 0.020856$
- $[Ca^{2+}]_i = 0.000049$
- Excitatory Synapses:
  Rising time constant $= 2.5$ ms
  Decaying time constant $= 5.6$ ms
  Reversal potential $= -7$ mV

Sources: Chen et al. (1999), Schild et al. (1993), Wang & Bradley (1995).

Acknowledgments

I thank N. T. Carnevale for help with the simulations using NEURON. I would also acknowledge a number of valuable comments from P. Di Lorenzo, J. Victor, and C. Assisi. This study was supported by NIDCD grant RO1-DC006914 to P. Di Lorenzo.

References

Agmon-Snir, H., Carr, C. E., & Rinzel, J. (1998). The role of dendrites in auditory coincidence detection. *Nature*, *393*, 268–272.

Ariav, G., Polsky, A., & Schiller, J. (2003). Submillisecond precision of the input-output transformation function mediated by fast sodium dendritic spikes in basal dendrites of CA1 pyramidal neurons. *J. Neurosci.*, *23*(21), 7750–7758.

Benson, D. L., Colman, D. R., & Huntley, G. W. (2001). Molecules, maps and synapse specificity *Nat. Rev. Neurosci.*, *2*, 899–909.

Carter, A. G., Soler-Llavina, G. J., & Sabatini, B. L. (2007). Timing and location of synaptic inputs determine modes of subthreshold integration in striatal medium spiny neurons. *J. Neurosci.*, *27*(33), 8967–8977.

Chen, C. Y., Horowitz, J. H., & Bonham, A. C. (1999). A presynaptic mechanism contributes to depression of autonomic signal transmission in NTS. *Am. J. Physiol.*, *277*, H1350–H1360.

Cline, H. T. (2001). Dendritic arbor development and synaptogenesis. *Curr. Opin. Neurobiol.*, *11*, 118–126.

Di Lorenzo, P. M., & Victor, J. D. (2003). Taste response variability and temporal coding in the nucleus of the solitary tract of the rat. *J. Neurophysiol.*, *90*, 1418–1431.

Di Lorenzo, P. M., Chen, J.-Y., & Victor, J. D. (2009). Quality time: Representation of a multidimensional sensory domain through temporal coding. *J. Neurosci., 29*(9), 9227–9238.

Euler, T., Detwiler, P. B., & Denk W. (2002). Directionally selective calcium signals in dendrites of starburst amacrine cells. *Nature*, *418*, 845–852.

Gao, F.-B. (2007). Molecular and cellular mechanisms of dendritic morphogenesis. *Curr. Opin. Neurobiol.*, *17*, 1–8.

Gao, F.-B., Brenman, J. E., Jan, L. Y., & Jan, Y.-N. (1999). Genes regulating dendritic outgrowth, branching, and routing in Drosophila. *Gene Dev.*, *13*, 2549–2561.

Gasparini, S., & Magee, J. C. (2006). State-dependent dendritic computation in hippocampal CA1 pyramidal neurons. *J. Neurosci.*, *26*(7), 2088–2100.

Gasparini, S., Migliore, M., & Magee, J. C. (2004). On the initiation and propagation of dendritic spikes in CA1 pyramidal neurons. *J. Neurosci.*, *24*(49), 11046–11056.

Gulledge, A. T., Kampa, B. M., & Stuart, G. J. (2005). Synaptic integration in dendritic trees. *J. Neurobiol.*, *64*, 75–90.

Hines M. L., & Carnevale, N. T. (1997). The NEURON simulation environment. *Neural Comp.*, *9*, 1179–1209.

Jan, Y.-N., & Jan, L. Y. (2003). The control of dendritic development. *Neuron*, *40*, 229–242.

Joris, P. X., Smith, P. H., & Yin, C. T. (1998). Coincidence detection in the auditory system: 50 years after Jeffres. *Neuron*, *21*, 1235–1238.

Kruskal, J. B., & Wish, M. (1978). *Multidimensional scaling*. Beverly Hills, CA: Sage.

Lestienne, R. (2001). Spike timing, synchronization and information processing on the sensory side of the central nervous system. *Prog. Neurobiol.*, *65*, 545–591.

Mainen, Z. F., & Sejnowski, T. R. (1996). Influence of dendritic structure on firing pattern in model neocortical neurons. *Nature*, *382*, 363–366.

Maletic-Savatic, M., Lenn, N. J., & Trimmer, J. S. (1995). Differential spatiotemporal expression of K^+ channel polypeptides in rat hippocampal neurons developing in situ and in vitro. *J Neurosci.*, *15*, 3840–3851.

McAllister, A. K. (2000). Cellular and molecular mechanisms of dendrite growth. *Cereb. Cortex*, *10*, 963–973.

Miyashita, T., & Kubo, Y. (1997). Localization and developmental changes of the expression of two inward rectifying K^+ channel proteins in the rat brain. *Brain Res.*, *750*, 251–263.

Poirazi, P., Brannon, T., & Mel, B. W. (2003). Arithmetic of subthreshold synaptic summation in a model CA1 pyramidal cell. *Neuron*, *37*, 977–987.

Polsky, A., Mel, B. W., & Schiller, J. (2004). Computational subunits in thin dendrites of pyramidal cells. *Nat. Neurosci.*, *7*(6), 621–627.

Reyes, A. (2001). Influence of dendritic conductances on the input-output properties of neurons. *Annu. Rev. Neurosci.*, *24*, 653–675.

Roussin, A. T., Victor, J. D., Chen, J.-Y., & Di Lorenzo, P. M. (2008). Variability in responses and temporal coding of tastants of similar quality in the nucleus of the solitary tract of the rat. *J. Neurophysiol.*, *99*(2), 644–655.

Schild, J. H., Khushalani, S., Clark, J. W., Andresen, M. C., Kunze, D. L., & Yang, M. (1993). An ionic current model for neurons in the rat medial nucleus tractus solitary receiving sensory afferent input. *J. Physiol.*, *469*, 341–363.

Scott, E. K., & Luo, L. (2001). How do dendrites take their shape? *Nat. Neurosci.*, *4*(4), 359–365.

Shen, K. (2004). Molecular mechanisms of target specificity during synapse formation. *Curr. Opin. Neurobiol.*, *14*, 83–88.

Shen, K., & Bargmann, C. I. (2003). The immunoglobulin superfamily protein SYG-1 determines the location of specific synapses in *C. elegans*. *Cell*, *112*, 619–630.

Singer, W. (1999). Neuronal synchrony: A versatile code for the definition of relations? *Neuron*, *24*, 49–65.

Smith, D. J., & Rubel, E. W. (1979). Organization and development of brain stem auditory nuclei of the chicken: Dendritic gradients in nucleus laminaris. *J. Comp. Neurol.*, *186*, 213–239.

Somogyi, P., Tamas, G., Lujan, R., & Buhl, E. H. (1998). Salient features of synaptic organization in the cerebral cortex. *Brain Res. Rev.*, *26*, 113–135.

Stopfer, M., & Laurent, G. (1999). Short-term memory in olfactory network dynamics. *Nature*, *402*, 664–668.

Tukker, J. J., Taylor, W. R., & Smith, R. G. (2004). Direction selectivity in a model of the starburst amacrine cell. *Visual Neurosci.*, *21*, 611–625.

Vanay, D. I., & Taylor, W. R. (2002). Direction selectivity in the retina. *Curr. Opin. Neurobio.*, *12*, 405–410.

Victor, J. D. (2005). Spike train metrics. *Curr. Opin. Neurobiol.*, *15*(5), 585–592.

Victor, J. D., & Purpura K. P. (1996). Nature and precision of temporal coding in visual cortex: A metric-space analysis. *J. Neurophysiol.*, *76*, 1310–1326.

Victor, J. D., & Purpura K. P. (1997). Metric-space analysis of spike trains: Theory, algorithms, and application. *Network*, *8*, 127–164.

Wang, L., & Bradley, R. M. (1995). In vitro study of afferent synaptic transmission in the rostral gustatory zone of the rat nucleus of the solitary tract. *Brain Res.*, *702*, 188–198.

Wong, R. O. L., & Ghosh, A. (2002). Activity-dependent regulation of dendritic growth and patterning. *Nat. Rev. Neurosci.*, *3*, 803–812.

Received November 18, 2008; accepted July 17, 2009.